Extended state observer-based robust non-linear integral dynamic surface control for triaxial MEMS gyroscope

Mehran Hosseini-Pishrobat and Jafar Keighobadi*

Faculty of Mechanical Engineering, University of Tabriz, 29 Bahman, Tabriz P.C. 5166614766, Iran. E-mail: m.hoseini92@ms.tabrizu.ac.ir

(Accepted October 8, 2018)

SUMMARY

This paper reports an extended state observer (ESO)-based robust dynamic surface control (DSC) method for triaxial MEMS gyroscope applications. An ESO with non-linear gain function is designed to estimate both velocity and disturbance vectors of the gyroscope dynamics via measured position signals. Using the sector-bounded property of the non-linear gain function, the design of an \mathcal{L}_2 -robust ESO is phrased as a convex optimization problem in terms of linear matrix inequalities (LMIs). Next, by using the estimated velocity and disturbance, a certainty equivalence tracking controller is designed based on DSC. To achieve an improved robustness and to remove static steady-state tracking errors, new non-linear integral error surfaces are incorporated into the DSC. Based on the energy-to-peak ($\mathcal{L}_2 - \mathcal{L}_{\infty}$) performance criterion, a finite number of LMIs are derived to obtain the DSC gains. In order to prevent amplification of the measurement noise in the DSC error dynamics, a multi-objective convex optimization problem, which guarantees a prescribed $\mathcal{L}_2 - \mathcal{L}_{\infty}$ performance bound, is considered. Finally, the efficacy of the proposed control method is illustrated by detailed software simulations.

KEYWORDS: Triaxial MEMS gyroscope; Dynamics surface control; Extended state observer; Linear matrix inequality.

1. Introduction

MEMS gyroscopes, as micromachined inertial sensors, are used for measuring the angular velocity of an object with respect to a non-rotating reference frame. The application areas of these sensors are quite vast, ranging from inertial navigation, automobile safety systems, and robotics to consumer electronics and sports. 1-3 The main advantages of MEMS gyroscopes over the conventional gyroscopes are miniaturized size, low weight, low power consumption, and capability to be integrated with electronics on the same chip.^{2,3} Besides, current micromachining technologies allow batch production of MEMS gyroscopes with low per device costs.³ Triaxial MEMS gyroscopes are variants of MEMS gyroscopes, which by using a single proof mass, are capable of angular velocity detection about three mutually orthogonal axes.^{4,5} The striking features of a triaxial gyroscope structure are the reduction of the footprint size, improvement of the productivity, and removing the need for accurate calibration of three separate sensors. ^{5,6} Moreover, using a single proof mass eliminates the mechanical interferences existing in the conventional multiple mass systems like inertial measurement units.⁶ Despite the aforementioned merits, miniaturized size, environmental variations, and imperfections of fabrication methods impose limiting effects on the performance of a MEMS gyroscope.⁷ For consistent operation of a MEMS gyroscope, it is necessary to generate and maintain a constant linear momentum in its structure through electrostatic actuation forces. Environmental variations and structural defects can degrade the performance of conventional open-loop operation modes for linear momentum regulation, resulting in inaccurate gyroscope outputs. 8 Accordingly, for high performance-demanding

^{*} Corresponding author. E-mail: Keighobadi@tabrizu.ac.ir

applications, a control system is required to guarantee the stability and robustness of the MEMS gyroscope. In recent years, various control methods such as adaptive control, 9,10 sliding mode control, 11 active disturbance rejection control, 12 and model predictive control have been considered for MEMS gyroscopes. Compared to the conventional MEMS gyroscopes, the role of control in triaxial gyroscopes is much more prominent due to their involved dynamics. The control problem of triaxial gyroscopes has been also considered in the literature. John and Vinay designed a model reference adaptive controller, which drives the gyroscope vibration to a three-dimensional Lissajous trajectory. The controller requires measurement of both position and velocity of the gyroscope's proof mass. Fang *et al.* proposed an adaptive fuzzy controller for robust vibration control of the triaxial gyroscope. Based on the Lyapunov analysis, a fuzzy approximation and an adaptive control law are combined to compensate for the uncertainty. Song *et al.* designed a fuzzy logic-based adaptive dynamic surface controller for a triaxial gyroscope considering the dead-zone and saturation input non-linearities. 15

Dynamic surface control (DSC) is a recursive and systematic design method for robust control of uncertain non-linear dynamic systems. ^{16,17} DSC evolved from the conventional backstepping control to remedy the issue of the explosion of terms, which is a result of consecutive differentiations of auxiliary control variables. ^{16,17} In this regard, DSC introduces a series of low-pass filters into the backstepping control design. DSC provides an effective framework for controlling mechanical systems using the convex optimization-based robust control techniques. ^{18,19} This allows formulation of the control objectives in terms of linear matrix inequalities (LMIs) which can be solved very efficiently by convex programming software. Despite its merits, there are some drawbacks associated with the conventional DSC. The use of linear error surfaces in the conventional DSC makes it stability very sensitive to the variations of the control gains and may raise static tracking errors in the controlled output. ^{20,21} To circumvent these issues and to enhance the robustness of the DSC, we propose a new design method employing integral terms of suitable non-linear functions of tracking errors.

Extended state observers (ESOs) are a class of observers that, in addition to the state variables of a given system, estimate the disturbances affecting the system dynamics.²² Such disturbances, in general, represent the discrepancy between the underlying system and its mathematical model, including structural variations, unknown external inputs, and noises. ESOs can estimate a wide class of disturbances and, therefore, are powerful tools for disturbance rejection.²²

The focus of this paper is to propose a control method for stable and robust operation of a triaxial MEMS gyroscope in the presence of parametric uncertainty, external disturbances, and noises. For this purpose, we consider a tracking control problem for the proof mass vibration to obtain a suitable level of the linear momentum. As the main contribution, we combine the merits of both DSC and ESO-based disturbance rejection techniques to achieve a robust tracking control of the triaxial gyroscope. The novelties of this control method are pointed out as follows:

- The existing control methods for triaxial gyroscopes require full state measurement of the system, which includes detection of both position and velocity of the proof mass. However, our proposed method merely uses the position measurement, which is more practical and related to the real working conditions of the sensor. Moreover, we consider the issue of measurement noise in the control design.
- We design an ESO with a non-linear gain function for robust estimation of both velocity and disturbance vectors of the gyroscope system. Using the sector-bounded description of the gain function, we phrase the ESO design in terms of a finite number of LMIs. To adjust a trade-off between the measurement noise amplification and estimation accuracy, we propose a convex optimization problem based on \mathcal{L}_2 -performance.
- For tracking control of the gyroscope, we design a non-linear dynamic surface controller that uses the output of the ESO as well as the measured position signals. By using suitable non-linear integral terms in the DSC error surfaces, the proposed controller can handle static tracking errors and large perturbation due to low-pass filters and ESO estimation errors. To achieve an optimal robust performance, using the energy-to-peak criterion, we formulate the design of the DSC gains in terms of a finite number of LMIs. Moreover, to prevent the amplification of the measurement noise in the DSC error dynamics, we propose a multi-objective convex optimization problem.

The rest of this paper is structured as follows. In Section 2, the mathematical model of a triaxial MEMS gyroscope and its control problem are explained. In Section 3, an ESO is designed to estimate

Table I. Key symbols used for the description of the MEMS gyroscope dynamics.

Symbol	Meaning	
\overline{m}	Proof mass	
k_{11}, k_{22}, k_{33}	Linear stiffness constants along \tilde{E}_1 , \tilde{E}_2 and \tilde{E}_3 directions, respectively	
k_{12}, k_{13}, k_{23}	Cross-coupling stiffness constants	
d_{11}, d_{22}, d_{33}	Damping constants along \tilde{E}_1 , \tilde{E}_2 and \tilde{E}_3 directions, respectively	
d_{12}, d_{13}, d_{23}	Cross-coupling damping constants	
$\alpha_1, \alpha_2, \alpha_3$	Coefficients of cubic stiffness nonlinearities along \tilde{E}_1 , \tilde{E}_2 and \tilde{E}_3 directions, respectively	
$\omega_1, \omega_2, \omega_3$	Coordinates of the angular velocity in the $\tilde{\mathcal{I}}$ frame	
u_1, u_2, u_3	Electrostatic control forces along \tilde{E}_1 , \tilde{E}_2 and \tilde{E}_3 directions, respectively	

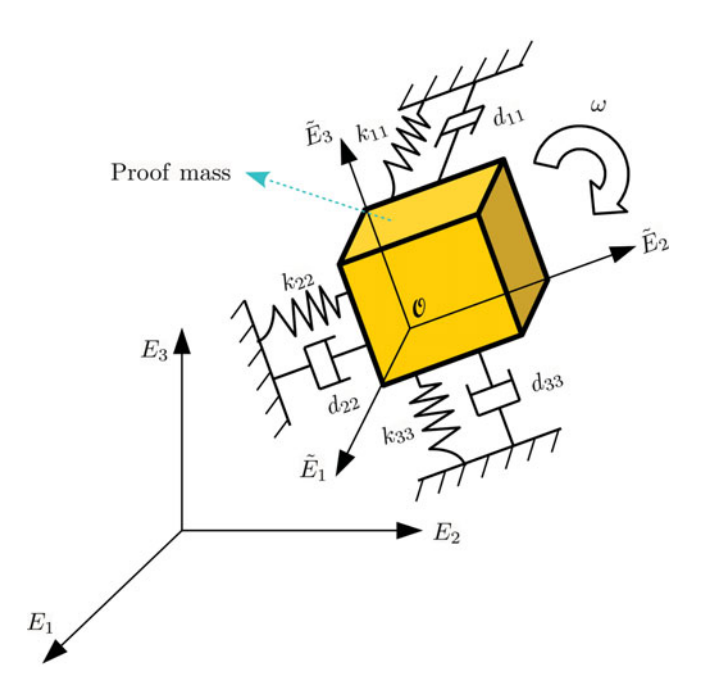


Fig. 1. Schematics of a triaxial MEMS gyroscope.

the unmeasured velocity vector as well as the disturbance vector of the gyroscope system. Next, in Section 4, a non-linear integral dynamic surface controller is proposed to achieve robust tracking control of the gyroscope. Simulation results are discussed in Section 5, and, finally, concluding remarks are given in Section 6.

Notation: Throughout the paper, the notation $\|.\|$ stands for the 2-norm of a vector/matrix. The zero and identity matrices of compatible dimensions are denoted by O and I, respectively. For a symmetric matrix $P \in \mathbb{R}^{n \times n}$, the notation P > 0 (≥ 0) implies that P is positive definite (positive semi-definite). Similarly, P < 0 (≤ 0) implies that P is negative definite (negative semi-definite). For a signal $x(.) \in \mathbb{R}^n$, the \mathcal{L}_2 and \mathcal{L}_∞ norms are defined as $\|x\|_{\mathcal{L}_2} := \sqrt{\int_0^\infty \|x(t)\|^2} \, dt$ and $\|x\|_{\mathcal{L}_\infty} := \sup_{t \in \mathbb{R}^+} \|x(t)\|$, respectively. For a $s \in \mathbb{R}$, the hyperbolic tangent function is given by, $\tanh(s) = \exp(2s) - 1$ / $(\exp(2s) + 1)$.

2. Description of MEMS Gyroscope Mathematical Model and Its Control Problem

The mechanical model of a MEMS gyroscope is represented as a three-degrees-of-freedom vibrating system (see Fig. 1 for details and Table I for the symbols). To describe the dynamics of the gyroscope, we consider two Cartesian reference frames $\mathcal{I} = (E_1, E_2, E_3)$ and $\tilde{\mathcal{I}} = (\tilde{E}_1, \tilde{E}_2, \tilde{E}_3)$. The reference $\mathcal{I} = (E_1, E_2, E_3)$ is fixed in an inertial space, whereas $\tilde{\mathcal{I}} = (\tilde{E}_1, \tilde{E}_2, \tilde{E}_3)$ is a body frame, rigidly attached to the gyroscope. The origin of $\tilde{\mathcal{I}}$ frame, point \mathcal{O} , is placed on the free position of the proof

mass and its axes are aligned with the nominal axes of the sensor. We assume that the acceleration of the point $\mathcal O$ with respect to the inertial frame $\mathcal I$ is negligible. The motion of the proof mass in the reference frame $\tilde{\mathcal I}=(\tilde E_1,\tilde E_2,\tilde E_3)$ is described by the displacement components q_1,q_2 , and q_3 along the respective axes. The frame $\tilde{\mathcal I}$ is subjected to an angular velocity $\omega\colon\mathbb R^+\to\mathbb R^3$, with respect to the inertial frame $\mathcal I$. Using either Newtonian or Lagrangian formalism, we obtain the dynamic equations of the gyroscope, with respect to the $\tilde{\mathcal I}$ frame, as follows:

$$M\ddot{q} + D\dot{q} + Kq + G(q) = u + 2m\Omega\dot{q} + m(\dot{\Omega} - \Omega^2)q, \tag{1}$$

where $q \triangleq [q_1, q_2, q_3]^{\top} \in \mathbb{R}^3$ is the vector of generalized coordinates, $u \triangleq [u_1, u_2, u_3]^{\top} \in \mathbb{R}^3$ is the control vector, $M \in \mathbb{R}^{3 \times 3}$ is the mass matrix, $D \in \mathbb{R}^{3 \times 3}$ is the damping matrix, $K \in \mathbb{R}^{3 \times 3}$ is the linear stiffness matrix, $G : \mathbb{R}^3 \to \mathbb{R}^3$ is a non-linear function standing for the cubic stiffness terms caused by mid-plane stretching effects, $u_3 \to \mathbb{R}^3$ and $u_3 \to \mathbb{R}^3$ is a skew-symmetric matrix associated with the angular velocity vector. These matrices are given by

$$M = \begin{bmatrix} m & 0 & 0 \\ 0 & m & 0 \\ 0 & 0 & m \end{bmatrix}, D = \begin{bmatrix} d_{11} & d_{12} & d_{13} \\ d_{12} & d_{22} & d_{23} \\ d_{13} & d_{23} & d_{33} \end{bmatrix}, K = \begin{bmatrix} k_{11} & k_{12} & k_{13} \\ k_{12} & k_{22} & k_{23} \\ k_{13} & k_{23} & k_{33} \end{bmatrix}, G(q) = \begin{bmatrix} \alpha_1 q_1^3 \\ \alpha_2 q_2^3 \\ \alpha_3 q_3^3 \end{bmatrix},$$

$$\Omega = \begin{bmatrix} 0 & \omega_3 & -\omega_2 \\ -\omega_3 & 0 & \omega_1 \\ \omega_2 & -\omega_1 & 0 \end{bmatrix}.$$

Since the parameters of a MEMS gyroscope have very different scales, we normalized the equation of motion (1). To this end, setting q_0 and w_0 as the reference length and the reference frequency, we use the following changes of variables:

$$\frac{q}{q_0} \to q, \ \frac{u}{mw_0q_0^2} \to u, \frac{D}{mw_0} \to D, \ \frac{K}{mw_0^2} \to K, \ \frac{\Omega}{w_0} \to \Omega, \ \frac{\alpha_iq_0^2}{mw_0^2} \to \alpha_i,$$

where $x' \to x$ means that the variable x is replaced by its normalized form x'. Considering the parametric uncertainty caused by the input angular velocity as well as variations of the environmental factors, the normalized dynamics of the gyroscope is governed by the following state-space equations:

$$\dot{X}_1 = X_2,$$

$$\dot{X}_2 = f(X_1, X_2) + u + \Delta(X_1, X_2, t),$$
(2)

where $X_1 = q$, $X_2 = \dot{q}$ and $f(X_1, X_2) \triangleq -DX_2 - KX_1 - G(X_1)$. The function $\Delta : \mathbb{R}^3 \times \mathbb{R}^3 \times \mathbb{R}^4 \to \mathbb{R}^3$, which groups the disturbances, is given by

$$\Delta(X_1, X_2, t) \triangleq -(\delta D - 2\Omega)X_2 - (\delta K - \dot{\Omega} + \Omega^2)X_1 - \delta G(X_1) + \zeta(t), \tag{3}$$

where $\delta D \in \mathbb{R}^{3\times3}$, $\delta K \in \mathbb{R}^{3\times3}$, and $\delta G(X_1) \in \mathbb{R}^3$ represent the parameter variations, and $\zeta(.) \in \mathbb{R}^3$ models external disturbance inputs. Regarding the commonly used capacitive sensing technology, we consider the position vector of the proof mass, with respect to the frame $\tilde{\mathcal{I}}$, as the measured output of the MEMS gyroscope dynamic system. Accordingly, we consider the following output equation for the system (2):

$$Y = X_1 + \nu(t),\tag{4}$$

where $v(.) = [v_1(.), v_2(.), v_3(.)]^{\top} \in \mathbb{R}^3$ accounts for the measurement noise.

In order for a MEMS gyroscope to provide a consistent estimation of an input angular velocity, its mechanical structure should maintain a constant linear momentum with respect to the body frame $\tilde{\mathcal{I}}$. By the Coriolis effect, this constant linear momentum gives information about the input angular velocity. According to the Eqs. (2) and (4), the gyroscope dynamics is subject to parametric uncertainty,

external disturbances, and measurement noises. Therefore, a feedback controller is required to guarantee the robustness of the gyroscope system against these factors. In this regard, we consider the robust operation of the gyroscope as a tracking control problem. If the trajectory of the gyroscope's proof mass, along each vibration axis, tracks a given reference trajectory with the predefined amplitude and frequency, then the constant linear momentum condition will be satisfied. We should note that in this paper, our focus is on the robust tracking control of the gyroscope and the problem of angular velocity estimation is not considered. Effectively, after achieving the tracking control, the components of the angular velocity vector can be identified by either demodulation or optimal parameter estimation techniques. ^{11,13}

3. Extended State Observer Design

The basic aim of the ESO is to estimate both velocity signal, $X_2(.)$ and disturbance signal, $\Delta(t) \triangleq \Delta(X_1(t), X_2(t), t)$. To this end, the common method in the literature is to model the disturbance by an integral action, that is, $\dot{\Delta}(t) = 0.2$ In this paper, to improve the convergence of the disturbance estimation, we consider a more generic disturbance model of the form

$$\dot{X}_3 = SX_3,
\Delta(t) = FX_3,$$
(5)

where $X_3(.) \in \mathbb{R}^n$ is the state vector of the disturbance model and the matrices $S \in \mathbb{R}^{n \times n}$ and $F \in \mathbb{R}^{3 \times n}$ satisfy the following conditions:

- 1. The spectrum of the matrix S belongs to the imaginary axis in such a way that in the respective minimal polynomial, each eigenvalue has the multiplicity of one. This condition ensures the boundedness of $X_3(.)$ in both forward and backward times.
- 2. The pair (F, S) is observable.

Based on the disturbance model (5), we propose the following ESO:

$$\dot{\hat{X}}_{1} = \hat{X}_{2} + L_{1}\phi(Y - \hat{X}_{1}),
\dot{\hat{X}}_{2} = f(Y, \hat{X}_{2}) + u + F\hat{X}_{3} + L_{2}\phi(Y - \hat{X}_{1}),
\dot{\hat{X}}_{3} = S\hat{X}_{3}(t) + L_{3}\phi(Y - \hat{X}_{1}),$$
(6)

where \hat{X}_i denotes the estimate of X_i , L_i , for i = 1, 2, 3, are design matrices of suitable dimensions, and $\phi \colon \mathbb{R}^3 \to \mathbb{R}^3$ is a non-linear gain function defining the observer innovation process. To reach a compromise between the estimation convergence and the sensitivity to the measurement noise, we consider the following gain function for $\chi = [\chi_1, \chi_2, \chi_3] \in \mathbb{R}^3$:

$$\phi(\chi) = [\phi_1(\chi_1), \phi_2(\chi_2), \phi_3(\chi_3)]^\top,$$

$$\phi_i(\chi_i) \triangleq \chi_i + \frac{\varepsilon - 1}{2} (|\chi_i + d| - |\chi_i - d|),$$
(7)

where $0 < \varepsilon < 1$, and d > 0 are design parameters. The function $\phi_i(\chi_i)$ defines a dead-zone-type non-linearity in which, the observer gain reduces as the estimation error falls within the interval [-d, d]. The gain function (7) satisfies the following sector-bounded property for all $\chi \in \mathbb{R}^3$:

$$(\phi(\chi) - \varepsilon \chi)^{\top} (\phi(\chi) - \chi) \le 0. \tag{8}$$

Using the estimation error $\eta \triangleq \operatorname{col}(X_1 - \hat{X}_1, X_2 - \hat{X}_2, X_3 - \hat{X}_3) \in \mathbb{R}^{n+6}$, we obtain the following error dynamics for the ESO (6):

$$\dot{\eta} = A_0 \eta - L \phi(C_0 \eta) + w,$$

$$p = C_p \eta,$$
(9)

where $p \in \mathbb{R}^{n_p}$ is the desired performance output of the error dynamics, C_p is a real matrix of suitable dimensions, and

$$A_{0} = \begin{bmatrix} O & I & O \\ O & -D & F \\ O & O & S \end{bmatrix}, L = \begin{bmatrix} L_{1} \\ L_{2} \\ L_{3} \end{bmatrix}, C_{0} = \begin{bmatrix} I & O & O \end{bmatrix},$$

$$w = \begin{bmatrix} -L_{1}(\phi(C_{0}\eta + \nu) - \phi(C_{0}\eta)) \\ K\nu + G(X_{1} + \nu) - G(X_{1}) - L_{2}(\phi(C_{0}\eta + \nu) - \phi(C_{0}\eta)) \\ -L_{3}(\phi(C_{0}\eta + \nu) - \phi(C_{0}\eta)) \end{bmatrix}.$$

With a given gain function (7), we design the ESO (6) under the following specifications:

- (S1) The error dynamics (9) with w = 0 is globally exponentially stable.
- (S2) To make the desired output p insensitive to the perturbation w, the \mathcal{L}_2 -gain inequality $||p||_{\mathcal{L}_2} < \gamma ||w||_{\mathcal{L}_2}$ holds for a given scalar $\gamma > 0$, under zero initial conditions.

Theorem 1. For a non-linear gain function (7) with given parameters and a desired \mathcal{L}_2 -gain bound $\gamma > 0$, assume there exist a positive definite matrix $P \in \mathbb{R}^{(n+6)\times(n+6)}$, a matrix $\Upsilon \in \mathbb{R}^{(n+6)\times 3}$, and a scalar $\varrho > 0$ satisfying the following LMI:

$$\begin{bmatrix} PA_0 + A_0^{\top} P + C_p^{\top} C_p - \varrho \varepsilon C_0^{\top} C_0 & -\Upsilon + \varrho \left(\frac{1+\epsilon}{2}\right) C_0^{\top} & P \\ -\Upsilon^{\top} + \varrho \left(\frac{1+\epsilon}{2}\right) C_0 & -\varrho I & O \\ P & O & -\gamma^2 I \end{bmatrix} < 0.$$
 (10)

Then, the error dynamics (9) with $L = P^{-1}\Upsilon$ satisfies both (S1) and (S2).

Proof. If there exists a positive definite function $V(e) = \eta^{\top} P \eta$ satisfying

$$\frac{\mathrm{d}V(\eta)}{\mathrm{d}t} + p^{\top}p - \gamma^2 w^{\top}w < 0, \tag{11}$$

then both (S1) and (S2) are satisfied.²⁴ Moreover, the sector-bounded property (8) implies that the following inequality should be considered:

$$(\phi(C_0\eta) - \varepsilon C_0\eta)^{\top} (\phi(C_0\eta) - C_0\eta) \le 0. \tag{12}$$

According to the S-procedure,²⁴ the inequality (11) holds for all e and $\phi(C_0e)$ satisfying (12) if there exists a scalar $\varrho > 0$ for which

$$\frac{\mathrm{d}V(\eta)}{\mathrm{d}t} + p^{\mathsf{T}}p - \gamma^2 w^{\mathsf{T}}w - \varrho(\phi(C_0\eta) - \varepsilon C_0\eta)^{\mathsf{T}}(\phi(C_0\eta) - C_0\eta) < 0. \tag{13}$$

From (13), we obtain the quadratic inequality

$$\eta^{\top} (PA_0 + A_0^{\top}P + C_p^{\top}C_p)\eta - 2\eta^{\top}PL\phi(C_0\eta) + 2\eta^{\top}Pw - \gamma^2w^{\top}w$$
$$- \varrho(\phi^{\top}(C_0\eta)\phi(C_0\eta) + \varepsilon\eta^{\top}C_0^{\top}C_0\eta - (1+\varepsilon)\eta^{\top}C_0^{\top}\phi(C_0\eta)) < 0,$$

which is equivalent to the LMI (10) with $\Upsilon \triangleq PL$.

The induced \mathcal{L}_2 -gain of the system (9) can be obtained by minimizing γ^2 subject to the conditions of Theorem 1. However, it should be noted that, to achieve a smaller \mathcal{L}_2 -gain bound, a larger norm of the matrix L is required. Considering the components of the disturbance w, this results in amplification of the measurement noise. To achieve a trade-off between the \mathcal{L}_2 disturbance attenuation and sensitivity to the measurement noise, the norm of L should be constrained to an acceptable range. More specifically, we require that $\|P^{-1}\| \leq \beta_1$ and $\|\Upsilon\| \leq \beta_2$ so that $\|L\| \leq \beta_1\beta_2$ for the given positives β_1 and β_2 . We formulate this requirement, in terms of LMIs, as follows:

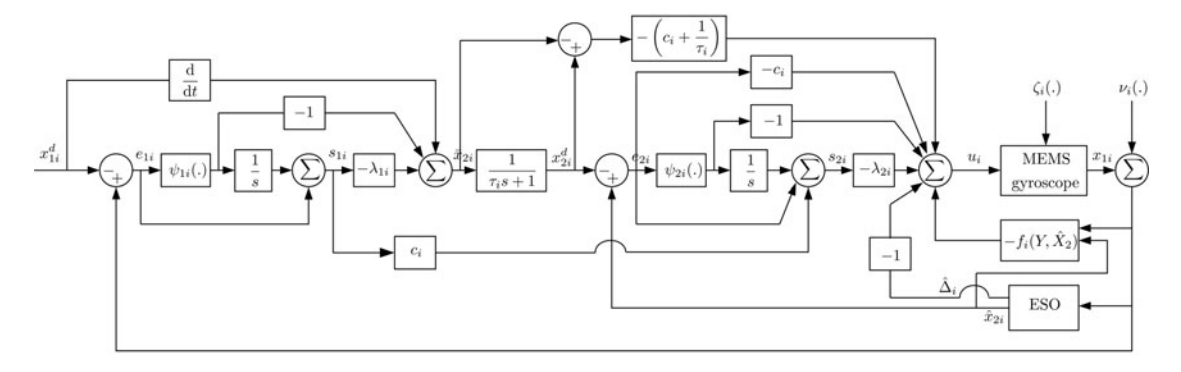


Fig. 2. Block diagram of the proposed non-linear integral dynamic surface control system.

- 1. Since $||P^{-1}|| = 1/\lambda_{\min}(P)$, the condition $||P^{-1}|| \le \beta_1$ implies that $\lambda_{\min}(P) \ge \beta_1^{-1}$ or equivalently $P \beta_1^{-1}I \ge 0$.
- 2. Since $\|\Upsilon\| = \sqrt{\lambda_{\max}(\Upsilon^{\top}\Upsilon)}$, the condition $\|\Upsilon\| \leq \beta_2$ implies that $\lambda_{\max}(\Upsilon^{\top}\Upsilon) \leq \beta_2^2$ or equivalently $\Upsilon^{\top}\Upsilon \beta_2^2 I \leq 0$. Therefore, according to the Schur complement, we have

$$\begin{bmatrix} -\beta_2^2 I & \Upsilon^\top \\ \Upsilon & -I \end{bmatrix} \le 0. \tag{14}$$

Based on the above reasoning, the following convex optimization is proposed for the ESO design: given $\beta_1 > 0$ and $\beta_2 > 0$ solve

minimize
$$\gamma^2$$

subject to $P - \beta_1^{-1}I \ge 0$, $\varrho > 0$, and LMIs (10) and (14). (15)

4. Non-Linear Integral Dynamic Surface Control

In this section, we design a non-linear integral DSC system that uses the measurement signals of the gyroscope together with the output of the ESO (6) to regulate the gyroscope vibration. Figure 2 shows the block diagram of the closed-loop ESO–DSC system. Corresponding to each degree-of-freedom, we rewrite the gyroscope dynamics (2) in the following decomposed form:

$$\dot{x}_{1i} = x_{2i},
\dot{x}_{2i} = f_i(X_1, X_2) + u_i + \Delta_i(X_1, X_2, t),$$
(16)

where x_{1i}, x_{2i} , and $\Delta_i(.)$, for i=1,2,3, denote the ith components of X_1, X_2 , and $\Delta(.)$, respectively. As stated in Section 2, the control goal is to asymptotically track a desired vibration trajectory $x_{1i}^d(.) \in \mathbb{R}$ by x_{1i} , for i=1,2,3. We assume that the signals $x_{1i}^d(.), \dot{x}_{1i}^d(.)$, and $\ddot{x}_{1i}^d(.)$ all are bounded and available for control purposes. We perform the DSC design by the following steps:

Step 1: We define the first tracking error $e_{1i} \in \mathbb{R}$ and the first error surface $s_{1i} \in \mathbb{R}$, respectively, as

$$e_{1i} \stackrel{\triangle}{=} x_{1i} - x_{1i}^d, \tag{17}$$

$$s_{1i} \triangleq e_{1i} + \int_0^t \psi_{1i}(e_{1i}(\varsigma)) \,\mathrm{d}\varsigma, \tag{18}$$

where the non-linear function $\psi_{2i}(.) \in \mathbb{R}$ is defined as follows with κ_{1i} , $\rho_{1i} \ge 0$, and $\varepsilon_{1i} > 0$ being design parameters:

$$\psi_{1i}(e_{1i}) \triangleq \kappa_{1i}e_{1i} + \rho_{1i}\tanh\left(\frac{e_{1i}}{\varepsilon_{1i}}\right). \tag{19}$$

The dynamics of the first error surface is given by

$$\dot{s}_{1i} = x_{2i} - \dot{x}_{1i}^d + \psi_{1i}(e_{1i}). \tag{20}$$

Regarding $x_{2i} = \bar{x}_{2i}$ as a synthetic input, we consider the following input to stabilize (20):

$$\bar{x}_{2i} = \dot{x}_{1i}^d - \psi_{1i}(e_{1i}) - \lambda_{1i}s_{1i}, \tag{21}$$

where $\lambda_{1i} > 0$ is a design parameter. To avoid the problem of explosion of terms, we pass \bar{x}_{2i} through the following low-pass filter with the time constant $\tau_i > 0$:

$$\tau_i \dot{x}_{2i}^d + x_{2i}^d = \bar{x}_{2i}, \ x_{2i}^d(0) = \bar{x}_{2i}(0). \tag{22}$$

Step 2: We define the second tracking $e_{2i} \in \mathbb{R}$ and the second error surface $s_{2i} \in \mathbb{R}$, respectively, as

$$e_{2i} \stackrel{\triangle}{=} x_{2i} - x_{2i}^d, \tag{23}$$

$$s_{2i} \triangleq c_i s_{1i} + e_{2i} + \int_0^t \psi_{2i} (e_{2i}(\varsigma)) d\varsigma,$$
 (24)

where $c_i \ge 0$ and the non-linear function $\psi_{1i}(.) \in \mathbb{R}$ is defined as follows for design parameters κ_{2i} , $\rho_{2i} \ge 0$, and $\varepsilon_{2i} > 0$:

$$\psi_{2i}(e_{2i}) \triangleq \kappa_{2i}e_{2i} + \rho_{2i}\tanh\left(\frac{e_{2i}}{\varepsilon_{2i}}\right).$$
 (25)

By differentiating s_{2i} with respect to time, we obtain

$$\dot{s}_{2i} = -c_i \lambda_{1i} s_{1i} + c_i e_{2i} + \psi_{2i}(e_{2i}) + \left(c_i + \frac{1}{\tau_i}\right) \left(x_{2i}^d - \bar{x}_{2i}\right) + f_i(X_1, X_2) + u_i + \Delta_i(t).$$
(26)

To stabilize the dynamics of s_{2i} , the following control input is considered:

$$u_{i} = -c_{i}\hat{e}_{2i} - \psi_{2i}(\hat{e}_{2i}) - \left(c_{i} + \frac{1}{\tau_{i}}\right)\left(x_{2i}^{d} - \bar{x}_{2i}\right) - f_{i}(Y, \hat{X}_{2}) - \hat{\Delta}_{i}(t) - \lambda_{2i}\hat{s}_{2i}, \tag{27}$$

where $\lambda_{2i} > 0$ is a design parameter and

$$\hat{e}_{2i} \triangleq \hat{x}_{2i} - x_{2i}^d, \tag{28}$$

$$\hat{s}_{2i} \triangleq c_i s_{1i} + \hat{e}_{2i} + \psi_{2i}(\hat{e}_{2i}), \tag{29}$$

with $\hat{\Delta}_i$ and \hat{x}_{2i} being the *i*th components of $F\hat{X}_3$ and \hat{X}_2 , respectively.

Remark 1. According to the error surfaces (18) and (24), the first components of the functions $\psi_{1i}(.)$ and $\psi_{2i}(.)$ produce linear integral action terms that reject static errors effectively, especially those may caused by the low-pass filters.²⁰ The second components produce non-linear integral terms that improve the robustness of the controller against perturbations.²¹ Moreover, the employed hyperbolic tangent function can be interpreted as a continuous approximation of the integral of the signum of the error which is used for the robust control of uncertain non-linear systems.^{25,26}

Remark 2. The constant $c_i \ge 0$ in (24) provides a recursive design of the error surfaces via a linear coupling term. Liu *et al.*²¹ has shown that such a coupling term can improve the convergence and the robustness of the DSC.

Remark 3. By setting $c_i = 0$, $\kappa_{1i} = \kappa_{2i} = 0$, and $\rho_{1i} = \rho_{2i} = 0$, the proposed non-linear integral DSC reduces to the conventional DSC, that is, $s_{1i} \equiv e_{1i}$ and $s_{2i} \equiv e_{2i}$. Therefore, our proposed method contains the conventional DSC as a special case.

Step 3: In this step, we study the dynamics of the error surfaces under the control law (27). To this end, using $\xi_i \triangleq x_{2i}^d - \bar{x}_{2i}$ as the filtering error of (22) and taking the effect of the measurement noise on \bar{x}_{2i} into account, we obtain the following augmented error surface dynamics:

$$\dot{s}_{ai} = A_i s_{ai} + \varpi_i,$$

 $z_i = C_z s_{ai}, \ i = 1, 2, 3,$ (30)

where $s_{ai} \triangleq [s_{1i}, s_{2i}, \xi_i]^{\top} \in \mathbb{R}^3$ is the augmented error vector, $\varpi_i = [\varpi_{i1}, \varpi_{i2}, \varpi_{i3}]^{\top} \in \mathbb{R}^3$ is the vector of perturbations and non-linearities, z_i is a desired performance output, C_z is a real matrix of compatible dimensions, and

$$\begin{split} A_i &= \begin{bmatrix} -(c_i + \lambda_{1i}) & 1 & 1 \\ -c_i \lambda_{1i} & -\lambda_{2i} & 0 \\ -\kappa_{1i}^2 - (\lambda_{1i} + \kappa_{1i})(c_i + \lambda_{1i}) & \lambda_{1i} + \kappa_{1i} & \lambda_{1i} + \kappa_{1i} - \frac{1}{\tau_i} \end{bmatrix}, \\ \varpi_{i1} &= -\lambda_{1i} \left(v_i + \int_0^t \left(\psi_{1i} \left(e_{1i}(\varsigma) + v_i(\varsigma) \right) - \psi_{1i} \left(e_{1i}(\varsigma) \right) \right) \mathrm{d}\varsigma \right) - \left(\psi_{1i} \left(e_{1i} + v_i \right) - \psi_{1i} \left(e_{1i} \right) \right) \\ &- \int_0^t \psi_{2i} \left(e_{2i}(\varsigma) \right) \mathrm{d}\varsigma, \\ \varpi_{i2} &= c_i \left(\varpi_{i1} + \int_0^t \psi_{2i} \left(e_{2i}(\varsigma) \right) \mathrm{d}\varsigma \right) + f_i(X_1, X_2) - f_i(Y, \hat{X}_2) + \Delta_i(t) - F \hat{X}_{3(i)} \\ &+ (c_i + \lambda_{2i})(x_{2i} - \hat{x}_{2i}) + (1 + \lambda_{2i}) \left(\psi_{2i}(e_{2i}) - \psi_{2i}(\hat{e}_{2i}) \right), \\ \varpi_{i3} &= (\lambda_{1i} + \kappa_{1i}) \varpi_{i1} - \dot{\varpi}_{i1} - \psi_{2i}(e_{2i}) + \rho_{1i} \frac{\mathrm{d}}{\mathrm{d}t} \left(\tanh \left(\frac{e_{1i}}{\varepsilon_{1i}} \right) \right) - \ddot{x}_{1i}^d \\ &+ \kappa_{1i}^2 \int_0^t \psi_{1i} \left(e_{1i}(\varsigma) \right) \mathrm{d}\varsigma - \kappa_{1i} \rho_{1i} \tanh \left(\frac{e_{1i}}{\varepsilon_{1i}} \right). \end{split}$$

For the sake of sequel design purposes, we consider the following decomposition of the matrix A_i , which separates contribution of λ_{1i} from λ_{2i} and τ_i :¹⁸

$$A_{i} = \bar{A}_{i} + B\Theta_{i}, \qquad (31)$$

$$\bar{A}_{i} = \begin{bmatrix}
-(c_{i} + \lambda_{1i}) & 1 & 1 \\
-c_{i}\lambda_{1i} & 0 & 0 \\
-\kappa_{1i}^{2} - (\lambda_{1i} + \kappa_{1i})(c_{i} + \lambda_{1i}) & \lambda_{1i} + \kappa_{1i} & \lambda_{1i} + \kappa_{1i}
\end{bmatrix}, B = \begin{bmatrix}
0 & 0 \\
0 & 1
\end{bmatrix},$$

$$\Theta_{i} = \begin{bmatrix}
0 & -\lambda_{2i} & 0 \\
0 & 0 & -\frac{1}{\tau_{i}}
\end{bmatrix}.$$

Step 4: In order to achieve stability as well as a robust performance, we design the non-linear integral DSC parameters under the following specifications:

(S3) The system (30) with $\varpi_i = 0$ is globally exponentially stable.

(S4) To attenuate the effect of ϖ_i on the performance output z_i , we impose the energy-to-peak criterion $\|z_i\|_{\mathcal{L}_{\infty}} < \mu \|\varpi_i\|_{\mathcal{L}_2}$ for a given scalar $\mu > 0$, under zero initial conditions.

Theorem 2. Consider the augmented error surfaces dynamics (30) and the given non-linear functions (19) and (25). For a given control gain $\lambda_{1i} > 0$, a given coupling constant $c_i \geq 0$, a given integral gain $\kappa_{1i} \geq 0$, and an energy-to-peak performance index $\mu > 0$, assume there exist a diagonal positive definite matrix $P_i \in \mathbb{R}^{3\times 3}$ and a scalar $\sigma > 0$ satisfying

$$\bar{A}_i P_i + P_i \bar{A}_i^{\top} - \sigma B B^{\top} + I < 0, \tag{32}$$

$$C_z P_i C_z^{\top} - \mu^2 I < 0,$$
 (33)

Then, the error dynamics (30) satisfies both (S3) and (S4) with $\Theta_i = -(\sigma/2)B^{\top}P_i^{-1}$.

Proof. For system (30), both (S3) and (S4) are satisfied if and only if there exists a $P_i > 0$ for which (see Theorem 4.6.2 of Skelton *et al.*²⁷)

$$(\bar{A}_i + B\Theta_i)P_i + P_i(\bar{A}_i + B\Theta_i)^\top + I < 0, \tag{34}$$

$$C_z P_i C_z^{\top} < \mu^2 I. \tag{35}$$

Using $\bar{\Theta}_i \triangleq \Theta_i P_i$, we rewrite the LMI (34) as

$$\bar{A}_i P_i + P_i \bar{A}_i^\top + B \bar{\Theta}_i + \bar{\Theta}_i^\top B^\top + I < 0. \tag{36}$$

In order to eliminate $\bar{\Theta}_i$, we invoke Finsler's lemma. ^{18,24} By this lemma, the LMI (36) is equivalent to the feasibility of the LMI (32) for a matrix $P_i > 0$ and a scalar $\sigma > 0$. Moreover, $\bar{\Theta}_i = -(\sigma/2)B^{\top}$ and therefore, $\Theta_i = -(\sigma/2)B^{\top}P_i^{-1}$. To obtain a gain matrix Θ_i with the structure of (31), the matrix P_i should be diagonal.

According to Theorem 2, we can calculate the induced $\mathcal{L}_2 - \mathcal{L}_\infty$ gain of the system (30) by solving the following convex optimization problem:

minimize
$$\mu^2$$

subject to $P_i > 0$ is diagonal, $\sigma > 0$, and LMIs (32) and (33). (37)

Achieving a smaller value for the energy-to-peak performance index requires larger values for the DSC gains. However, owing to the structure of the disturbance ϖ_i , large control gains cause an undesired amplification of the measurement noise in the DSC error dynamics. Thereby, we modify the optimization problem (37) in such a way that for given parameters λ_{1i} , c_i , and κ_{1i} the magnitudes of λ_{2i} and τ_i are properly constrained to prevent the measurement noise amplification. Since the norm of the matrix Θ_i depends on both σ and P_i^{-1} , a combination of σ and $-\lambda_{\min}(P_i)$ should be minimized. On this basis, we propose the following DSC design algorithm:

- 1. For given parameters, λ_{1i} , c_i , and κ_{1i} solve the optimization problem (37) to obtain the induced $\mathcal{L}_2 \mathcal{L}_{\infty}$ gain, μ^* .
- 2. Selecting a $\mu_m \ge \mu^*$ and a weighting parameter $0 \le \delta \le 1$, solve the following convex optimization problem to obtain λ_{2i} and τ_i :

minimize
$$\delta \sigma - (1 - \delta)\lambda_{\min}(P_i)$$

subject to $P_i > 0$ is diagonal, $\sigma > 0$, $\mu^2 - \mu_m^2 \le 0$, and LMIs (32) and (33). (38)

Step 5: In the last step, we show that the convergence of the error surface s_{1i} implies the convergence of the tracking error e_{1i} , which, in turn, results in the trajectory control of the gyroscope's proof mass.

Theorem 3. Consider the error surface s_{1i} defined by Eq. (18). Assume that the conditions of Theorem 2 are satisfied so that its results hold true. Then, the tracking error $e_{1i}(.)$ is globally bounded and globally ultimately bounded.

Parameter	MEMS gyroscope I	MEMS gyroscope II
m	$5.5680 \times 10^{-10} \text{ kg}$	$5.5207 \times 10^{-10} \text{ kg}$
k_{11}	2.6636 μN/μm	2.5743 μN/μm
k_{22}	$3.1897 \mu N/\mu m$	3.1657 μN/μm
k ₃₃	$3.8179 \mu N/\mu m$	3.8803 μN/μm
k_{12}	$0.0726 \ \mu N/\mu m$	$0.0702 \; \mu N/\mu m$
k_{23}	$0.1695 \mu N/\mu m$	0.1638 μN/μm
k_{13}	$0.1211 \mu \text{N}/\mu \text{m}$	0.1170 μN/μm
d_{11}	$3.6719 \times 10^{-9} \mu \text{Ns/} \mu \text{m}$	$3.5944 \times 10^{-9} \mu\text{Ns/}\mu\text{m}$
d_{22}	$3.0587 \times 10^{-9} \mu \text{Ns/} \mu \text{m}$	$2.9941 \times 10^{-9} \mu\text{Ns/}\mu\text{m}$
d_{33}	$2.8237 \times 10^{-9} \mu\text{Ns/}\mu\text{m}$	$2.7641 \times 10^{-9} \mu\text{Ns/}\mu\text{m}$
d_{12}	$1.1016 \times 10^{-10} \mu \text{Ns/} \mu \text{m}$	$1.0783 \times 10^{-10} \mu \text{Ns/} \mu \text{m}$
d_{23}	$1.8360 \times 10^{-10} \mu \text{Ns/} \mu \text{m}$	$1.7972 \times 10^{-10} \mu \text{Ns/} \mu \text{m}$
d_{13}	$3.3047 \times 10^{-10} \mu \text{Ns/} \mu \text{m}$	$3.2350 \times 10^{-10} \mu \text{Ns/} \mu \text{m}$
α_1	$0.1332 \mu \text{N}/\mu \text{m}^3$	$0.1287 \mu \text{N}/\mu \text{m}^3$
α_2	$0.1595 \mu \text{N}/\mu \text{m}^3$	$0.1583 \mu \text{N}/\mu \text{m}^3$
α_3	$0.1909 \ \mu \text{N}/\mu \text{m}^3$	$0.1940 \ \mu \text{N}/\mu \text{m}^3$

Table II. Simulation parameters of the triaxial MEMS gyroscopes^{5,6}.

Proof. From the definition of the error surface (18), we have the following dynamics for the tracking error:

$$\dot{e}_{1i} = -\psi_{1i}(e_{1i}) + \dot{s}_{1i}. \tag{39}$$

According to Theorem 2, $s_{1i}(.)$ is globally bounded and ultimately bounded. Therefore, it follows from the differential equation (30) that there exists a positive constant s_0 such that $\dot{s}_{1i}(.) \leq s_0$. Considering a candidate Lyapunov function of the form $\vartheta(e_{1i}) \triangleq e_{1i}^2/2$, we have

$$\dot{\vartheta}(e_{1i}) = -e_{1i}\psi_{1i}(e_{1i}) + e_{1i}\dot{s}_{1i}
\leq -\kappa_{1i}|e_{1i}|^2 - (\rho_{1i} - s_0)|e_{1i}| + \rho_{1i}\delta_0\varepsilon_{1i},$$
(40)

where $\delta_0 = 0.2785$. In the derivation of the differential inequality (40), we have used the well-known inequality, $|e_{1i}| - e_{1i} \tanh(e_{1i}/\epsilon_{1i}) \le \delta_0 \epsilon_{1i}$. Assuming that $\rho_{1i} > s_0$, we consider the compact set

$$\Lambda = \left\{ e_{1i} \in \mathbb{R} \mid |e_{1i}|^2 + \left(\frac{\rho_{1i} - s_0}{\kappa_{1i}} \right) |e_{1i}| \le \varepsilon_{1i} \frac{\rho_{1i} \delta_0}{\kappa_{1i}} \right\}. \tag{41}$$

Outside Λ , $\dot{\vartheta} < 0$, which means that any trajectory starting outside Λ will converge toward Λ . Moreover, on the boundary of Λ , $\dot{\vartheta} = 0$. Therefore, any trajectory starting inside Λ will remain in Λ . Based on this argument, all tracking error trajectories $e_{1i}(.)$ are globally bounded and globally ultimately bounded. Besides, the ultimate bound is proportional to $\sqrt{\epsilon_{1i}\rho_{1i}\delta_0/\kappa_{1i}}$.

Remark 4. According to the proof of Theorem 3, the smaller values of the parameter ϵ_{1i} result in the smaller ultimate bounds of the tracking error. In fact, by decreasing the values of ϵ_{1i} , the hyperbolic tangent function approaches the signum function and, consequently, generates a quasi-sliding motion in the DSC error surfaces.

5. Simulations

In order to assess the performance of the proposed control system, we carried out numerical simulations in the MATLAB/Simulink environment. To specify and solve the required LMI optimization problems, we used CVX, which is a specialized MATLAB package for solving convex programs.^{29,30} To show the applicability of the control method, we use two sets of triaxial MEMS gyroscope data provided by John.⁵ The data are acquired from finite element analysis-based optimizations which were performed

to obtain suitable triaxial gyroscope structures according to modal response, proof mass alignment, and the maximum allowable stress of the constituent material.⁵ The general specifications of the considered MEMS gyroscopes have been released as follows:⁵

- 1. The first triaxial gyroscope, referred as *MEMS gyroscope I*, utilizes a single suspension beam design and contains a silicone proof mass of dimensions $219.72 \times 219.72 \times 4.95 \mu m$. The gyroscope structure has the ratio of 1.09 between both the second-first and the third-second natural frequencies.
- 2. The second triaxial gyroscope, referred as *MEMS gyroscope II*, applies a double suspension beam design and a $228.45 \times 228.45 \times 4.54 \,\mu m$ silicon proof mass. The ratio between both the second-first and the third-second natural frequencies is 1.11.

Regarding the suspension structures of the gyroscopes, for a 1 μ m deflection, we assume that the forces generated by the non-linear stiffness are 5% of the linear parts. According to the damping and cross-coupling ratios given by John and Vinay,⁶ Table II gives the parameters of both MEMS gyroscopes I and II. Further details about the structural analysis and microfabrication techniques of these MEMS gyroscopes can be found in John⁵ and John and Vinay.⁶ For both MEMS gyroscopes, we consider the reference length, $q_0 = 1$ μ m and the reference frequency, $w_0 = 10$ kHz.

According to the MEMS gyroscope mathematical model governed by Eqs. (2)–(4), we consider the following uncertainty/disturbance specifications:

• Parametric uncertainty. For the input angular velocity, we consider time-varying signals of the form

$$\omega_1(t) = 5\cos(0.1w_0\pi t) \frac{\text{rad}}{\text{s}}, \ \omega_2(t) = 1 + 3\sin(0.12w_0\pi t) \frac{\text{rad}}{\text{s}},$$

$$\omega_3(t) = 2\sin(0.15w_0\pi t) + 3\cos(0.2w_0\pi t) \frac{\text{rad}}{\text{s}}.$$

According to Eq. (3), we assume that the gyroscopes parameters vary as $d_{ij} + \delta d_{ij}$, $k_{ij} + \delta k_{ij}$, and $\alpha_i + \delta \alpha_i$. Considering 3% variations from the nominal values, we consider the following parameter variations:

$$\delta k_{ij} = 0.03 k_{ij} \cos(w_0 t), \, \delta d_{ij} = 0.03 d_{ij} \cos(w_0 t), \, \delta \alpha_i = 0.03 \alpha_i \cos(w_0 t).$$

It should be noted that we use a relatively high-frequency term $\cos(w_0t)$ to fully investigate the robustness of the control system against parameters variations. In a physical gyroscope, the variation of parameters over time would be much slower.

• External disturbance. The basic mechanism of the external disturbance in a MEMS gyroscope, represented by $\zeta(.)$ in Eq. (3), is the mechanical—thermal noise. This noise is the result of the Brownian motion of the gas molecules around the proof mass. Along each axis of the gyroscope, we consider the respective disturbance signal $\zeta_i(.)$ as a zero-mean white noise with normal distribution and the power spectral density (PSD) of

$$S_i = 4k_BT_ad_{ii}$$

where $k_B = 1.38066 \times 10^{-23}$ J/K is the Boltzman constant and T_a is the ambient temperature, which is assumed to be 300 K.³¹

• Measurement noise. In a MEMS gyroscope, the electrical noises of the sensing circuit produce a disturbance in the measurements, represented by $\nu(.)$ in Eq. (4). The spectral power of this measurement noise depends on the ambient temperature and the parasitic capacitance of the sensing circuit. According to the noise analysis results of Park⁹ and Park and Horowitz, ¹⁰ for each axis of the gyroscope, we consider $\nu_i(.)$ as a zero-mean white noise with normal distribution and the PSD of $1.49 \times 10^{-15} \ \mu \text{m}^2 \text{s}$. In the simulations, this measurement noise resulted in a signal-to-noise ratio of about 85 dB.

The initial conditions for both MEMS gyroscopes I and II are $q(0) = [0.1, 0.1, 0.1]^{T}$ μ m and $\dot{q}(0) = [0, 0, 0]^{T}$ μ m/s. To control the gyroscope vibration in the resonance condition, we consider the

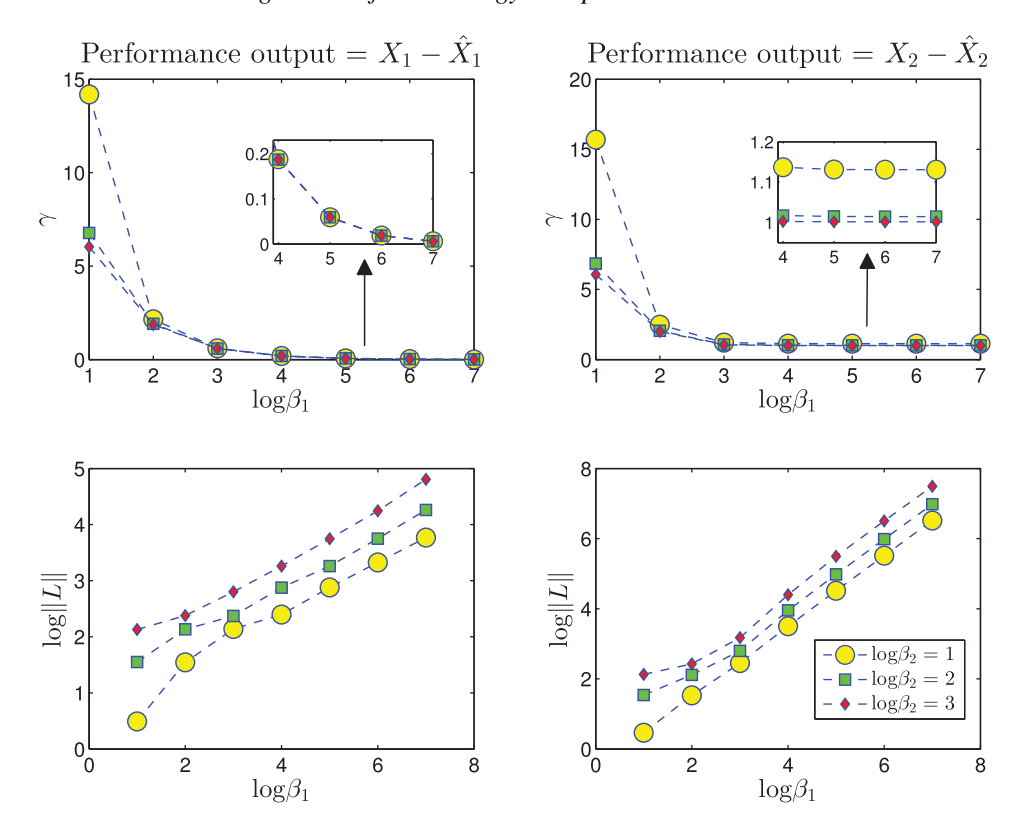


Fig. 3. Variations of \mathcal{L}_2 -performance index γ , and ||L|| vs. β_1 , β_2 for the ESO (6).

following Lissajous trajectory as the desired motion:

$$x_{1i}^d(t) = \sin\left(\sqrt{\frac{k_{ii}}{m}}t\right) \,\mu\text{m}, \text{ for } i = 1, 2, 3.$$
 (42)

We note that controlling a MEMS gyroscope in the resonance condition reduces the magnitudes of the required control forces.¹³ Regarding the desired trajectory (42), we consider the following matrices for the disturbance model (5):

$$S = \operatorname{diag}\left(\begin{bmatrix}0 & 1\\ -\frac{k_{11}}{m} & 0\end{bmatrix}, \begin{bmatrix}0 & 1\\ -\frac{k_{22}}{m} & 0\end{bmatrix}, \begin{bmatrix}0 & 1\\ -\frac{k_{33}}{m} & 0\end{bmatrix}\right), F = \begin{bmatrix}1 & 0 & 1 & 0 & 1 & 0\\ 1 & 0 & 1 & 0 & 1 & 0\\ 1 & 0 & 1 & 0 & 1 & 0\end{bmatrix}.$$

For the non-linear gain function (7), we use the parameter values $\varepsilon = 0.8$ and d = 0.1. In order to design the ESO (6), we solved the convex optimization problem (15) for $\beta_1 = 10^i$ and $\beta_2 = 10^j$. Through trial and error, we identified a feasibility range of i = 1:7 and j = 1:3. We considered two cases for the performance output of the ESO error dynamics (9): the position estimation error, $p = X_1 - \hat{X}_1$ and the velocity estimation error, $p = X_2 - \hat{X}_2$. Figure 3 shows the results of optimization problem (15) for the \mathcal{L}_2 -performance index γ and the ESO gain $\|L\|$. To save space, the results are only shown for the parameters of MEMS gyroscope I. Considering the parameters of MEMS gyroscope II, a similar figure is obtained. For a fixed value of β_2 , increasing β_1 results in a smaller value of γ , but, at the same time, increases the ESO gain. Additionally, for the performance output, $p = X_2 - \hat{X}_2$, $\|L\|$ has a larger increase rate. In the simulations, we considered the position estimation error as the performance variable and, by using $\beta_1 = 10^4$, $\beta_2 = 10$, we obtained the following results:

• For MEMS gyroscope I, the optimal \mathcal{L}_2 performance index is $\gamma = 0.1875$ with $\varrho = 624.9257$ and ||L|| = 249.8297.

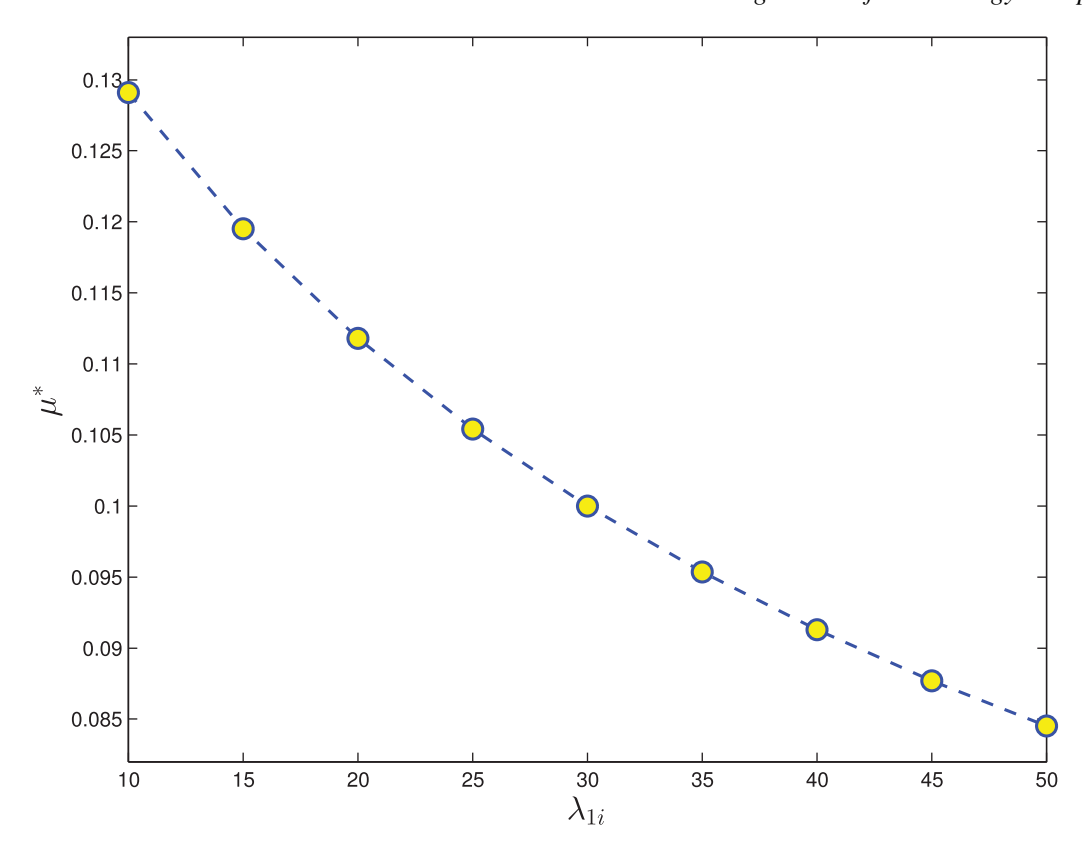


Fig. 4. Induced energy-to-peak gain μ^* vs. λ_{1i} .

• For MEMS gyroscope II, the optimal \mathcal{L}_2 performance index is $\gamma = 0.1900$ with $\varrho = 611.5340$ and ||L|| = 248.4295.

In order to design the non-linear integral DSC gains, first, we solved the optimization problem (37). Since the position tracking is the main control objective, we consider the DSC desired output as $z_i = s_{1i}$. The parameters of the functions $\psi_{1i}(.)$ and $\psi_{2i}(.)$ are selected as $\kappa_{1i} = 1$, $\kappa_{2i} = 0.1$, $\rho_{1i} = 1$, $\rho_{2i} = 0.5$, $\varepsilon_{1i} = \varepsilon_{2i} = 1/40$ and the coupling constant is $c_i = 20$. Figure 4 shows variations of the induced $\mathcal{L}_2 - \mathcal{L}_\infty$ gain μ^* for $\lambda_{1i} \in [10, 50]$. Next, by solving the optimization problem (38) with $\lambda_{1i} = 20$, $\delta = 0.68$, and $\mu_m = 0.13$, we got the following results:

$$P_i = \text{diag}(0.0125, 5.0005, 10.5124), \ \sigma = 466.2233, \ \mu = 0.1255, \ \lambda_{2i} = 46.6181, \ \tau_i = 0.0451.$$

For the purpose of comparison, we also consider a conventional DSC with linear error surfaces. Following the LMI optimization, we tuned the parameters of the conventional DSC as $\lambda_{1i} = 22$, $\lambda_{2i} = 35.2210$, and $\tau_i = 0.0109$.

5.1. Simulation results

Figure 5 illustrates the trajectory tracking performance of the control system. Figure 6 depicts the comparative graphs of the tracking errors e_{1i} , i = 1, 2, 3 of the proposed DSC and the conventional DSC. From these results, we observe that the error surfaces, after a very small settling time, converge to a small bounded neighborhood of the origin. Mathematically speaking, the steady-state tracking errors satisfy the following:

- MEMS gyroscope I: $|e_{1i}| \le 0.013~\mu \text{m}$ with the proposed DSC and $|e_{1i}| \le 0.043~\mu \text{m}$ with the conventional DSC.
- MEMS gyroscope II: $|e_{1i}| \le 0.014 \ \mu \text{m}$ with the proposed DSC and $|e_{1i}| \le 0.049 \ \mu \text{m}$ with the conventional DSC.

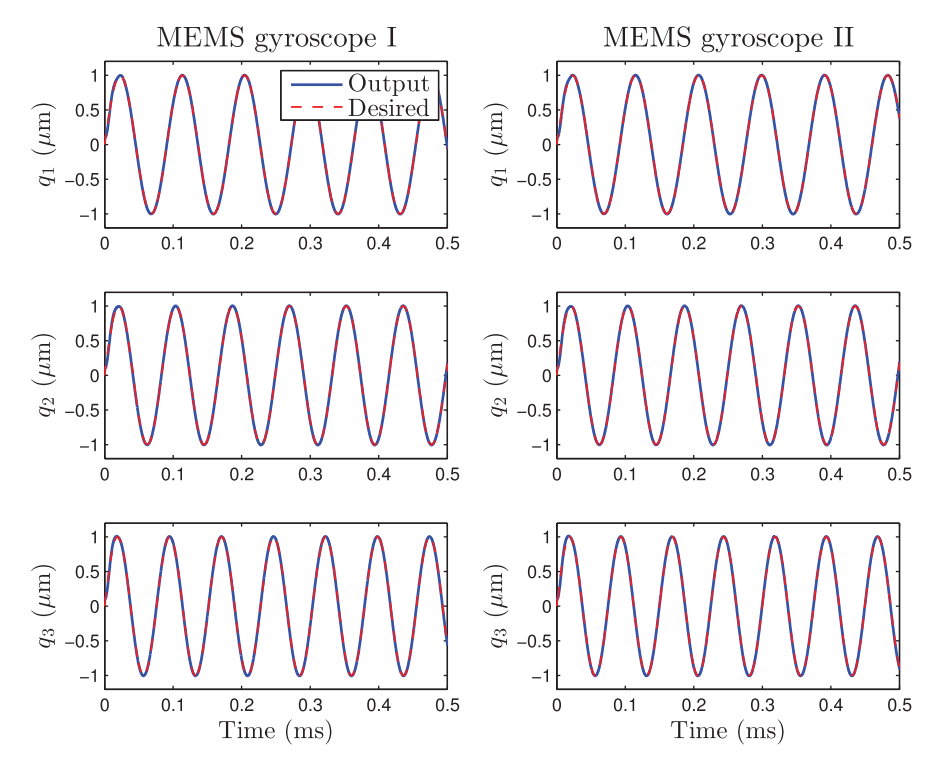


Fig. 5. Tracking behavior of the controlled gyroscope systems.

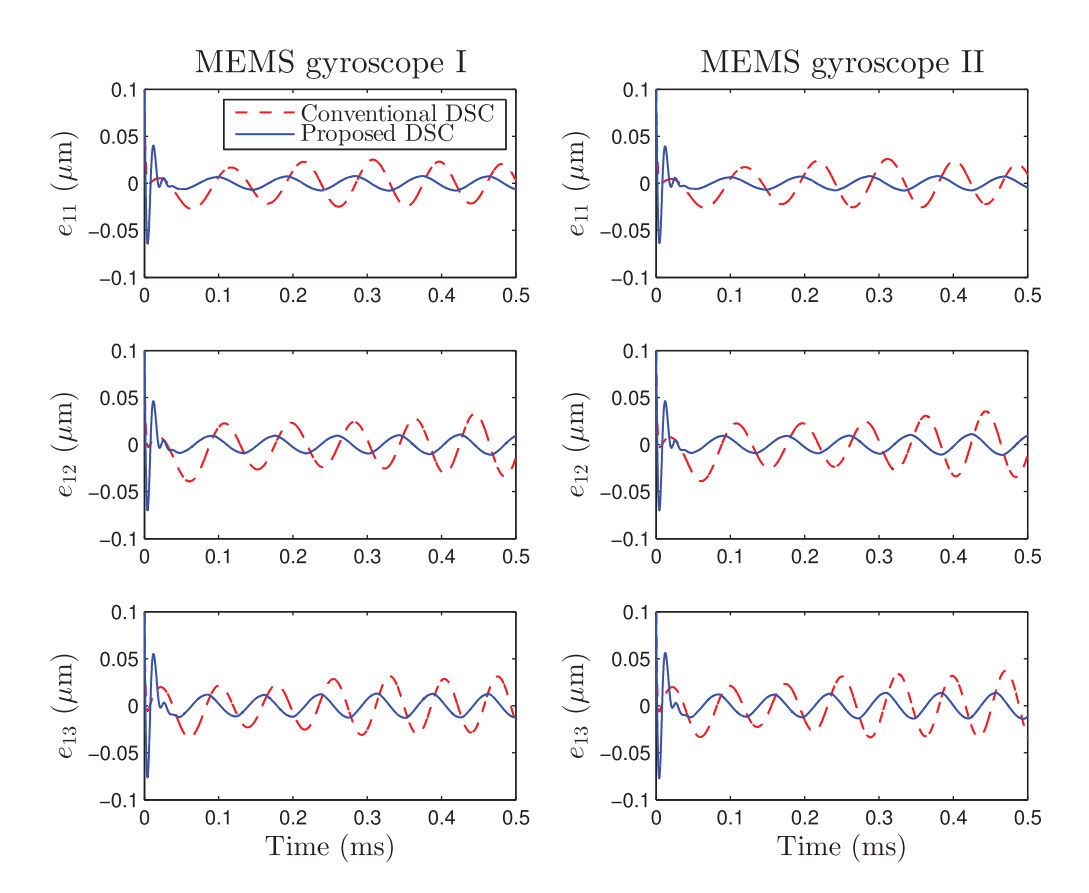


Fig. 6. Time trajectories of the tracking errors of the proposed DSC (solid lines) and the conventional DSC (dashed lines).

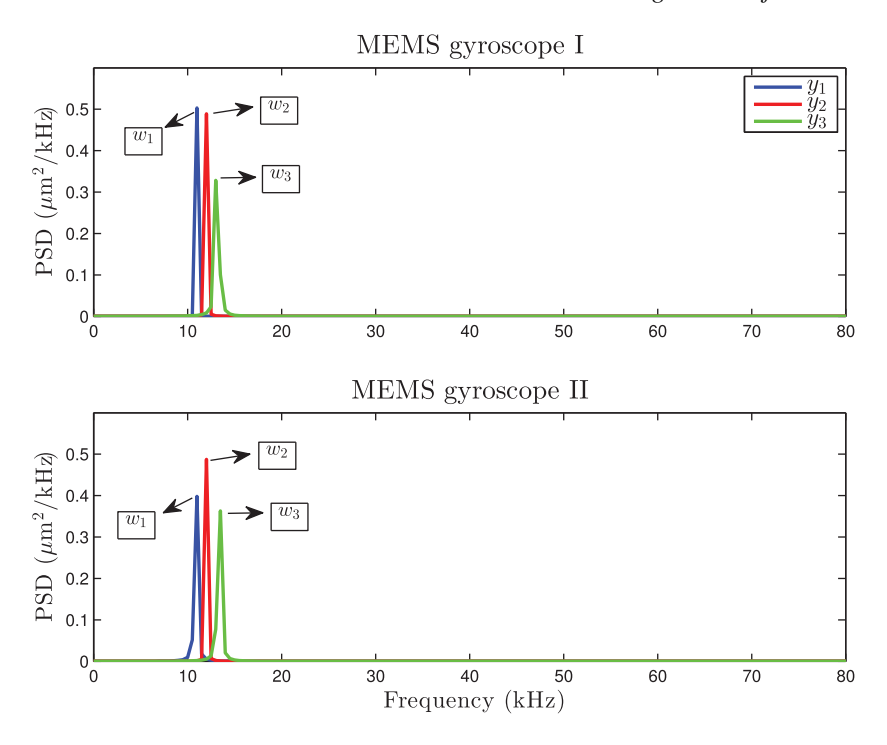


Fig. 7. Power spectral density of the measured outputs of the MEMS gyroscopes.

Therefore, the steady-state tracking error of the proposed DSC is below 1.4%, while that of the conventional DSC is 5%. This observation confirms that the proposed non-linear integral design considerably improves the robustness of the conventional DSC. We should note that even though the integral terms reduces the steady-state tracking error of the conventional DSC, the resulted integral action causes a slower transient response. Therefore, a trade-off between the steady-state tracking error and the transient response should be considered in the design. Figure 7 shows the power spectra of the measured outputs (that is, y_i) of the closed-loop MEMS gyroscopes. One can see that the main frequency content of the output signals corresponds to those of the desired signal (42). In the outputs, there are no shifts in the desired frequencies, which indicates that the control system compensates for the effect of stiffness non-linearity.²³ Besides, the control system successfully attenuates the effects of the parameters variations and high-frequency noises/disturbances on the gyroscope outputs. The force signals generated by the controller are shown in Fig. 8 for each axis of the gyroscope. These forces can be generated by the common electrostatic comb drive or parallel plate actuators.⁵ To examine the effects of the system disturbance, $\Delta(t) \triangleq \Delta(q(t), \dot{q}(t), t)$ and the measurement noise on the triaxial gyroscope vibration, we evaluate the following quantities:

$$\mathcal{G}_{\Delta \to q} \triangleq \left(\frac{\int_{0}^{T} \|q(t) - \bar{q}_{\Delta}(t)\|^{2} dt}{\int_{0}^{T} \|\Delta(t)\|^{2} dt} \right)^{\frac{1}{2}},
\mathcal{G}_{v \to q} \triangleq \left(\frac{\int_{0}^{T} \|q(t) - \bar{q}_{v}(t)\|^{2} dt}{\int_{0}^{T} \|v(t)\|^{2} dt} \right)^{\frac{1}{2}}, \tag{43}$$

where $\bar{q}_{\Delta}(t)$ and $\bar{q}_{\nu}(t)$ are the gyroscope trajectories under $\Delta(t) \equiv 0$ and $\nu(t) \equiv 0$, respectively. Table III presents the numerical values of the quantities (43) for a closed-loop operation time of T=2 ms. The quantities $\mathcal{G}_{\Delta\to q}$, and $\mathcal{G}_{\Delta\to q}$ allow us to obtain an energy measure of the impact of the disturbances and measurement noises on the nominal tracking performance of the control system.

Table III. Numerical results of the quantities $\mathcal{G}_{\Delta \to q}$ and $\mathcal{G}_{\nu \to q}$ for MEMS gyroscopes I and II over the operation time T = 2 ms.

Quantity	MEMS gyroscope I	MEMS gyroscope II
$\mathcal{G}_{\Delta o q}$ $\left(rac{\mu\mathrm{m}}{\mu\mathrm{N}} ight)$	0.0224	0.0233
$\mathcal{G}_{\nu o q} \left(\frac{\mu m}{\mu m} \right)$	0.7921	0.7884

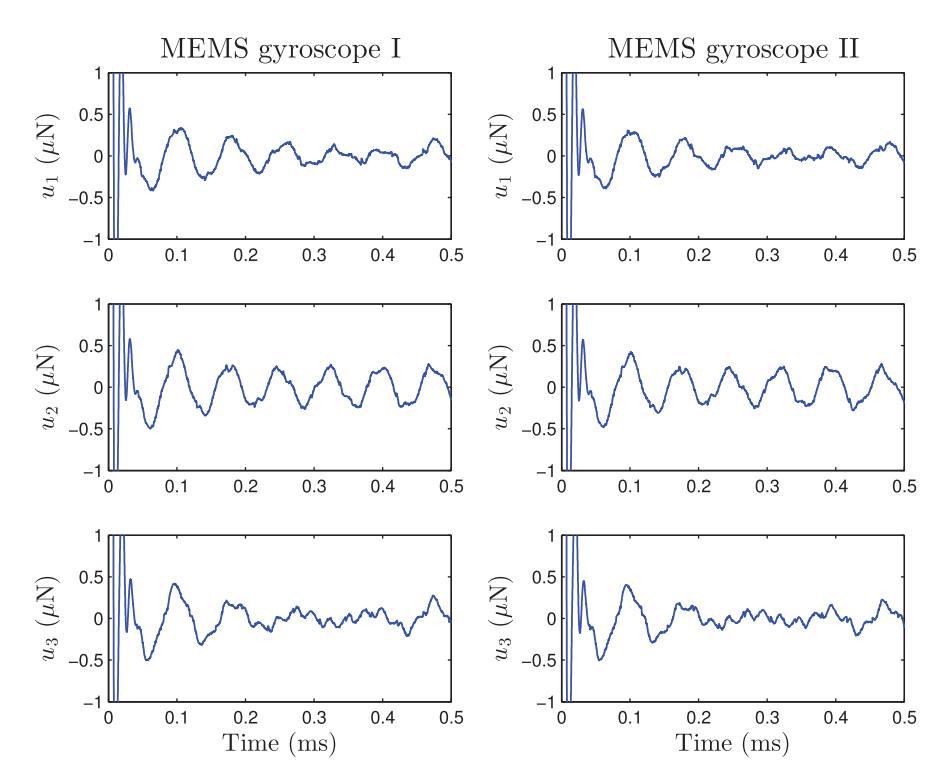


Fig. 8. Control signals generated by the controller.

In order to investigate the energy-to-peak performance of the DSC system, we define the following quantity under zero initial conditions:

$$\mu_i(T) \triangleq \frac{\sup_{0 \le t \le T} \|z_i(t)\|}{\left(\int_0^T \|\varpi_i(t)\|^2 dt\right)^{\frac{1}{2}}}, \text{ for } i = 1, 2, 3.$$
(44)

For a sufficiently large T > 0, $\mu_i(T)$ provides a suitable approximation of the energy-to-peak index μ . By taking T=2 ms, we obtained the following results, which show that the values of $\mu_i(T)$ are below the specified energy-to-peak index $\mu = 0.2$:

- MEMS gyroscope I: $\mu_1 = 8.9319 \times 10^{-4}$, $\mu_2 = 8.6213 \times 10^{-4}$, and $\mu_3 = 8.2998 \times 10^{-4}$. MEMS gyroscope II: $\mu_1 = 8.8866 \times 10^{-4}$, $\mu_2 = 8.5431 \times 10^{-4}$, and $\mu_3 = 8.2472 \times 10^{-4}$.

The overall results confirm that the proposed control system successfully tracks the desired trajectory for the gyroscope vibration. Besides, the robustness property of the control system significantly attenuates the effect of parameter uncertainty, disturbances, and noises. This, in turn, improves the stability and performance of the sensor in various environmental conditions.

To illustrate the performance of the ESO (6), Fig. 9 shows the estimation errors of the proof mass position and velocity signals. To save space, we only present the ESO results for MEMS gyroscope I, similar results are obtained for MEMS gyroscope II. After about 0.1 ms, the ESO estimation errors

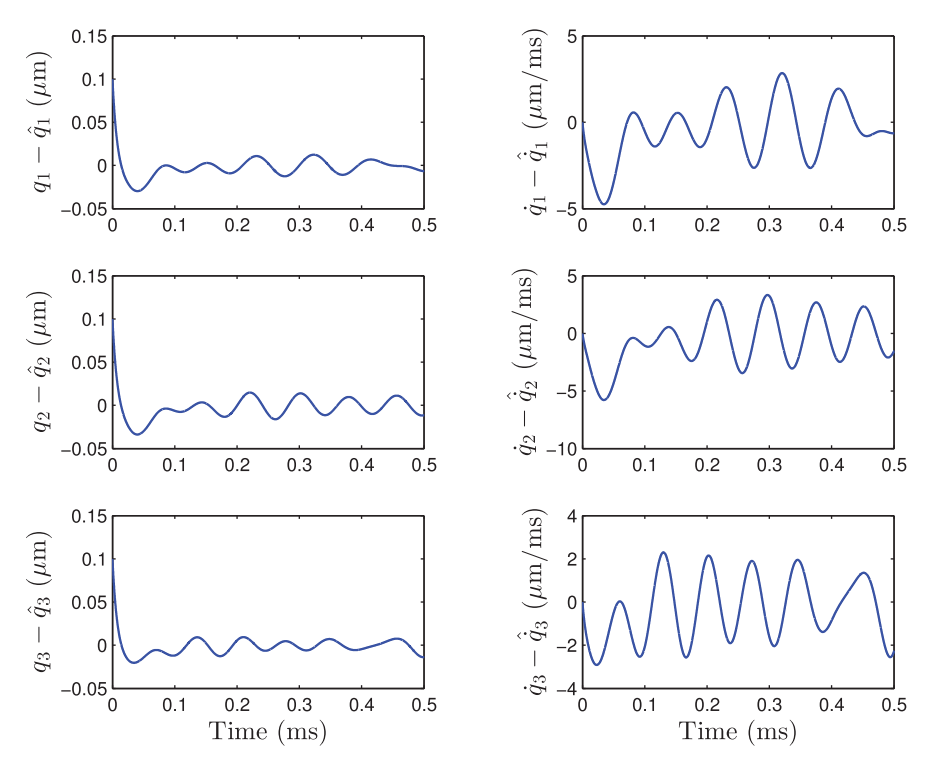


Fig. 9. Estimation errors of the ESO (6).

converge to a small bounded set around zero. In the steady-state, we get 2% and 5% maximum estimation errors for the position and the velocity signals, respectively.

In order to verify the \mathcal{L}_2 performance of the ESO, we consider the following quantity under zero initial conditions:

$$\gamma'(T) \triangleq \left(\frac{\int_0^T \|p(t)\|^2 dt}{\int_0^T \|w(t)\|^2 dt}\right)^{\frac{1}{2}}.$$
(45)

For a sufficiently large T>0, $\gamma'(T)$ provides a suitable approximation of the \mathcal{L}_2 performance index, γ . Setting T=2 ms, we obtained the following results, which show that the values of $\gamma'(T)$ are below the specified performance indices $\gamma=0.1875$ and $\gamma=0.1900$ for MEMS gyroscopes I and II, respectively:

- MEMS gyroscope I: $\gamma' = 0.0097$.
- MEMS gyroscope II: $\gamma' = 0.0101$.

5.2. Comparative study

To further investigate the advantages of the proposed controller, we compared its performance with the model reference adaptive controller, which has been proposed as a basic operation mode of a triaxial MEMS gyroscope.^{5,6} We should note that the adaptive control has been designed under different modeling assumptions. In particular, the effects of both mechanical—thermal and measurement noises, stiffness non-linearity, time-varying parameters variations, and the imperfect state measurement have not been considered. However, we first tuned a nominal adaptive controller, and then, we considered the effects of the uncertainty/disturbances. The control law of the model reference adaptive controller is

$$u = (\hat{D} - 2\hat{\Omega}) \dot{q}_m + \hat{R}q_m + u_0,$$

$$u_0 = -\Gamma(\dot{q} - \dot{q}_m),$$
(46)

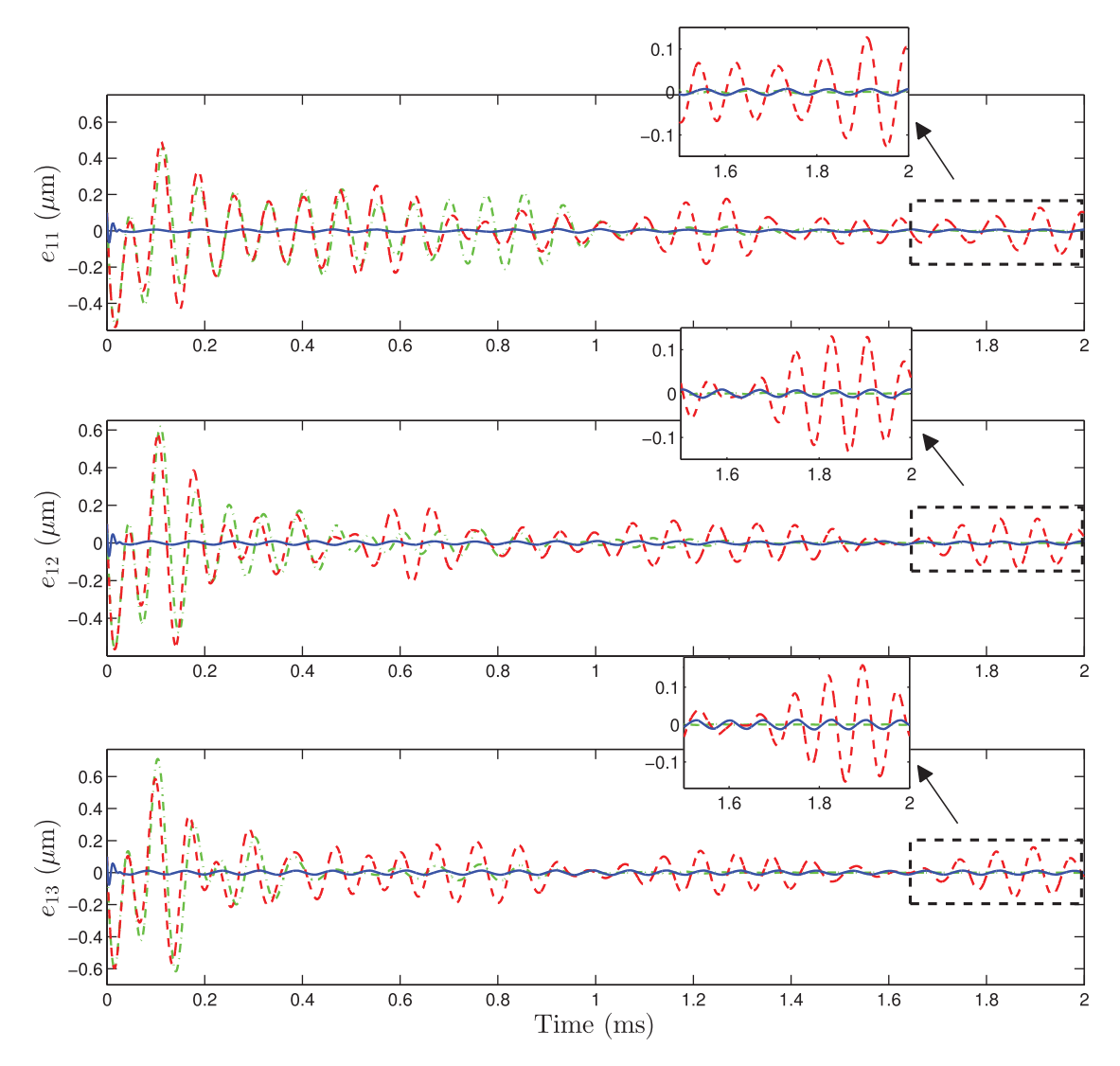


Fig. 10. Comparison of the tracking responses of the nominal adaptive controller (dash-dot lines), adaptive controller subject to uncertainty (dashed lines), and the proposed controller (solid lines).

where $q_m \in \mathbb{R}^3$ is the reference trajectory, $\Gamma \in \mathbb{R}^{3\times 3}$ is a design gain matrix, and the matrices \hat{R} , \hat{D} , $\hat{\Omega} \in \mathbb{R}^{3\times 3}$, are obtained from the following update laws with design positives γ_R , γ_D , γ_Ω :^{5,6}

$$\dot{\hat{R}} = \frac{1}{2} \gamma_R \left(u_0 \dot{q}_m^\top + \dot{q}_m u_0^\top \right),
\dot{\hat{D}} = \frac{1}{2} \gamma_D \left(u_0 \dot{q}_m^\top + \dot{q}_m u_0^\top \right),
\dot{\hat{\Omega}} = -\gamma_\Omega \left(u_0 \dot{q}_m^\top - \dot{q}_m u_0^\top \right).$$
(47)

The matrix \hat{R} is the estimate of the difference between stiffness matrices of the gyroscope K, and the reference model K_m . To remedy the issue of imperfect state measurement, we augment the following velocity observer to the adaptive controller:^{9,10}

$$\dot{\hat{q}}_p = \hat{q}_v + L(q - \hat{q}_p),
\dot{\hat{q}}_v = -K_m \hat{q}_p,$$
(48)

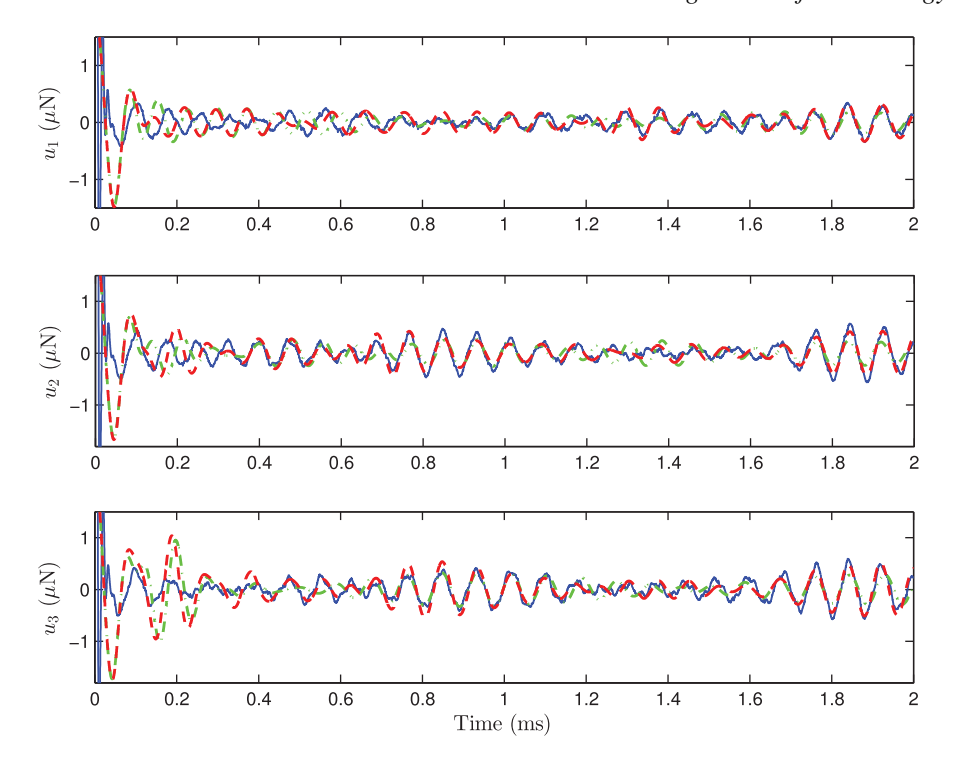


Fig. 11. Comparison of the control signals of the nominal adaptive controller (dash-dot lines), adaptive controller subject to uncertainty (dashed lines), and the proposed controller (solid lines).

where q_v is the estimate of \dot{q} , and $L \in \mathbb{R}^{3\times3}$ is a design gain matrix. Based on the nominal performance, we tuned the (normalized) parameters of the adaptive controller (46)–(47) and the velocity observer (48) as follows:

$$\Gamma = \text{diag}(4, 4, 4), \ L = \text{diag}(5, 5, 5), \ \gamma_R = \frac{1}{100}, \ \gamma_D = \frac{1}{100}, \ \gamma_\Omega = \frac{1}{400}.$$

For the sake of simplicity, we only present the comparison results of MEMS gyroscope I. Figures 10 and 11 show the comparative graphs of the tracking errors and the control signals along the three axes of the gyroscope, respectively. According to these figures, the adaptive controller has a much larger settling time (about 1 ms), and exhibits an oscillatory behavior in its transient phase. In the nominal case, the adaptive controller successfully achieves the steady-state tracking of the reference signal with a very small error. However, when the parametric uncertainty, non-linearities, and disturbances/noises affect the adaptive controller, its tracking performance significantly degrades. In the steady-state, the tracking errors of the proposed controller are below 1.4%, while those of the adaptive controller reach 15%. The control signals generated by the adaptive controller and the proposed controller converge to the approximately same steady-state waveform.

6. Conclusions

In this paper, the problem of robust control of a triaxial MEMS gyroscope was addressed using DSC and ESO. To improve the robustness of the conventional DSC, a new non-linear integral surface design was proposed. Using appropriate robust performance criteria, both DSC and ESO were designed through solving appropriate convex optimization problems. The proposed control system offers robustness against parameter variations, external disturbances, and measurement noises. By applying the ESO, only the position signal of gyroscope's proof mass is required to be measured in the control system. Detailed, comparative numerical simulations were conducted to illustrate the effectiveness of the control method. The results indicated robust and fast-tracking properties of the controller, which, in turn, regulates the gyroscope vibration and drives its linear momentum to the desired level. Estimation of the angular velocity vector using a parameter identifier coupled to the control system will be followed in the future studies.

References

- 1. P. Doostdar and J. Keighobadi, "Design and implementation of SMO for a nonlinear MIMO AHRS," Mech. Syst. Signal Process. **32**, 94–115 (2012).
- 2. J. Collin, P. Davidson, M. Kirkko-Jaakkola and H. Leppkoski, "Inertial Sensors and Their Applications," In: Handbook of Signal Processing Systems (S. S. Bhattacharyya, E. F. Deprettere, R. Leupers and J. Takala, eds.) (Springer, New York, NY, 2013) pp. 69-96.
- 3. G. Zhanshe, C. Fucheng, L. Boyu, C. Le, L. Chao and S. Ke, "Research development of silicon MEMS gyroscopes: A review," *Microsyst. Technol.* **21**(10), 2053–2066 (2015).

 N. Barbour and G. Schmidt, "Inertial sensor technology trends," *IEEE Sensors J.* **1**(4), 332–339 (2001).
- 5. J. D. John, Adaptively Controlled MEMS Triaxial Angular Rate Sensor PhD Thesis (School of Electrical and Computer Engineering, RMIT University, Melbourne, 2006).
- 6. J. D. John and T. Vinay, "Novel concept of a single-mass adaptively controlled triaxial angular rate sensor," IEEE Sensors J. 6, 588-595 (2006).
- 7. C. Acar and A. Shkel, MEMS Vibratory Gyroscopes: Structural Approaches to Improve Robustness (Springer, Boston, MA, 2009).
- C. Patel, P. McCluskey, "Performance Degradation of the MEMS Vibratory Gyroscope in Harsh Environments," Proceedings of the ASME. ASME International Mechanical Engineering Congress and Exposition, Volume 11: Nano and Micro Materials, Devices and Systems; Microsystems Integration, Denver, Colorado, USA (2011) pp. 511–515.
- S. Park, Adaptive Control Strategies for MEMS Gyroscopes *PhD Thesis* (U.C. Berkeley, Berkeley, CA, USA, 2000).
- 10. S. Park and R. Horowitz, "New Adaptive Mode of Operation for MEMS Gyroscopes," *J. Dyn. Syst. Meas. Control* **126**(4), 800–810 (2004).
- 11. C. Batur, T. Sreeramreddy and Q. Khasawneh, "Sliding mode control of a simulated MEMS gyroscope," ISA Trans. 45(1), 99–108 (2006).
- 12. Q. Zheng, L. Dong, D. H. Lee and Z. Gao, "Active disturbance rejection control for MEMS gyroscopes," IEEE Trans. Control Syst. Technol. 17(6), 1432–1438 (2009).
- 13. M. Hosseini-Pishrobat and J. Keighobadi, "Force-balancing model predictive control of MEMS vibratory gyroscope sensor," *Proc. Inst. Mech. Eng., Part C: J. Mech. Eng. Sci.* **230**(17), 3055–3065 (2016).
- 14. Y. Fang, J. Zhou and J. Fei, "Robust adaptive fuzzy controller with supervisory compensator for MEMS
- gyroscope sensor," *Robotica* **34**(10), 2330–2343 (2016).

 Z. Song, H. Li and K. Sun, "Adaptive dynamic surface control for MEMS triaxial gyroscope with nonlinear inputs," *Nonlinear Dyn.* **78**(1), 173–182 (2014).
- 16. D. Swaroop, J. K. Hedrick, P. P. Yip and J. C. Gerdes, "Dynamic surface control for a class of nonlinear systems," IEEE Trans. Autom. Control, 45(10), 1893-1899 (2000).
- 17. B. Song and J. K. Hedrick, Dynamic Surface Control of Uncertain Nonlinear Systems (Springer, London,
- 18. B. Song and J.K. Hedrick, "Design of dynamic surface control for fully-actuated mechanical systems," IFAC Proc. Vol. 44(1), 7363–7368 (2011).
- 19. B. Song, J. K. Hedrick and A. Howell, "Robust stabilization and ultimate boundedness of dynamic surface control systems via convex optimization," Int. J. Control, 75(12), 870–881 (2002)
- 20. L. Zhou, S. Fei and C. Jiang, "Adaptive integral dynamic surface control based on fully tuned radial basis function neural network," J. Syst. Eng. Electron. 21(6), 1072–1078 (2010).
- 21. X. Liu, X. Sun, S. Liu and S. Xu, "Nonlinear gains recursive sliding mode dynamic surface control with integral action," *Asian J. Control* 17(5), 1955–1961 (2015).
- 22. R. Madoski and P. Herman, "Survey on methods of increasing the efficiency of extended state disturbance observers," ISA Trans. 56, 18-27 (2015).
- 23. M.I. Younis, MEMS Linear and Nonlinear Statics and Dynamics (Springer, Boston, MA, 2011).
- 24. S. Boyd, L. E. Ghaoui, E. Feron and V. Balakrishnan, Linear Matrix Inequalities in System Control Theory, Society for Industrial and Applied Mathematics, (1994).
- 25. B. Xian, D. M. Dawson, M. S. deQueiroz and J. Chen "A continuous asymptotic tracking control strategy for uncertain nonlinear systems," IEEE Trans. Autom. Control 49(7), 1206–1206 (2004).
- 26. B. Zhao, B. Xian, Y. Zhang and X. Zhang, "Nonlinear robust adaptive tracking control of a quadrotor UAV via immersion and invariance methodology," *IEEE Trans. Ind. Electron.* **62**(5), 2891–2902 (2015).
- 27. R.E. Skelton, T. Iwasaki and K. M. Grigoriadis, A Unified Algebraic Approach to Linear Control Design (Taylor & Francis, London, 1997).
- 28. M. M. Polycarpou and P. A. Ioannou, "A robust adaptive nonlinear control design," Automatica 32(3), 423–427 (1996).
- 29. M. 1. Grant and S. Boyd, "Graph Implementations for Nonsmooth Convex Programs," In: Recent Advances in Learning and Control (V. D. Blondel, S. P. Boyd and H. Kimura, eds.) (Springer-Verlag Limited, 2008) pp. 95-110.
- 30. M. Grant, S. Boyd, "CVX: Matlab Software for Disciplined Convex Programming," version 2.1, cvxr.com/cvx, (2014).
- 31. V. Kempe, "Gyroscopes," In: Inertial MEMS: Principles and Practice (Cambridge University Press, Cambridge, 2011), pp. 364–459.